

Interacting Streams of Cognitive Active Agents in a Three-Way Intersection

Priyanka Iyer¹, Rajendra Singh Negi¹, Andreas Schadschneider²,
Gerhard Gompper^{1,2*}

^{1*}Theoretical Physics of Living Matter, Institute of Biological
Information Processing and Institute for Advanced Simulation,
Forschungszentrum Jülich, Jülich, 52425, Germany.

²Institute for Theoretical Physics, Universität zu Köln, Köln, 10587,
Germany.

*Corresponding author(s). E-mail(s): g.gompper@fz-juelich.de;
Contributing authors: p.iyer@fz-juelich.de; r.negi@fz-juelich.de;
as@thp.uni-koeln.de;

Abstract

The emergent collective motion of active agents - in particular pedestrians - at a three-way intersection is studied by Langevin simulations of cognitive intelligent active Brownian particles (iABPs) with directed visual perception and self-steering avoidance. Depending on the maneuverability Ω , the goal fixation K , and the vision angle ψ , different types of pedestrian motion emerge. At intermediate relative maneuverability $\Delta = \Omega/K$ and large ψ , pedestrians have noisy trajectories due to multiple scattering events as they encounter other pedestrians in their field of view. For $\psi = \pi$ and large maneuverability Δ , an effectively jammed state is found, which belongs to the percolation universality class. For small ψ , agents exhibit localised clustering and flocking, while for intermediate ψ self-organized rotational flows can emerge. Analysing the mean squared displacement and velocity auto-correlation of the agents revealed that the motion is well described by fractional Brownian Motion with positively correlated noise. Finally, despite the rich variety of collective behaviour, the fundamental flow diagram for the three-way-crossing setup shows a universal curve for the different vision angles. Our research provides valuable insights into the importance of vision angle and self-steering avoidance on pedestrian dynamics in semi-dense crowds.

Keywords: active Brownian particles, crowd dynamics, visual perception, self-steering

The understanding of collective pedestrian movement is imperative for the design of strategies facilitating smooth pedestrian flow in crowded areas, the mitigation of crowd-related disasters in confined spaces, and the development of evacuation procedures [1]. Here, an important aspect is the goal-oriented motion of all participants. For pedestrian navigation in crowds, typical scenarios are the formation of traffic jams in front of narrow passages and bottlenecks, the interaction of groups in counter flow leading to lane formation, and the self-organization of flows at intersections (see the reviews [2, 3] and references therein). Situations like the Shibuya Crossing in Tokyo or mall intersections pose important questions regarding self-organization and the design optimization of facilities. Experiments and simulations of bi-directional flows demonstrate lane formation [4–6], while cross flows at an angle result in stripe-like patterns [7]. Four-directional cross-flow experiments [8–11] and multi-directional crossing scenarios explored through circle antipode experiments [12, 13], with participants positioned on a circle and crossing diagonally, have been used to study navigation strategies, conflict avoidance etc.

The importance of understanding the flow of pedestrian crowds has led to the development of various modelling approaches in recent decades, e.g. the force-based models, cellular automaton-based approaches, several physics-inspired models, game theory, optimal control and fluid dynamics (for a more detailed exposition of the different approaches, see [2, 3, 14, 15] and references therein). The importance of a close interplay between empirical and theoretical investigations has inspired the use of specifically designed laboratory experiments [2, 3, 16], which generate quantitative results that are important benchmarks for modeling.

Collective pedestrian motion can be generically understood as the behavior of self-propelled interacting entities, which places it into the realm of the large field of “active matter” [17], which encompasses systems from suspensions cells and self-propelling colloids to schools of fish and flocks of birds. In this context, the active Brownian Particle (ABP) model has been used extensively to understand many intriguing aspects of non-equilibrium physics such as mobility-induced phase separation [18, 19] and wall accumulation [20, 21]. Moreover, when equipped with directional environment sensing and self-steering, ensembles of ‘intelligent’ ABP systems (iABPs) can show a rich variety of collective phenomena such as milling, single-file motion, flocking, worm-like swarms, and polar or nematic ordering [22–25]. In pedestrian models, vision-based sensing and cognitive steering are also key ingredients that determine the emergent collective behaviour [26–29], which suggests the applicability of iABP models for the description of pedestrian crowds [30].

Model and Cross-Stream Setup – We investigate here a three-stream intersection scenario [see Fig. 1(a)], which emulates a basic realization of multi-directional flows in a circle. In contrast to a straightforward two-way flow configuration, pedestrian movement at intersections with multiple streams does not readily organize itself through lane or stripe formation, making it an important case to study. A similar setup with two intersecting streams has been studied experimentally [8]. Since we are interested in the general physical mechanisms of interacting streams, sophisticated models, which usually have several adjustable parameters, are not appropriate. Instead, pedestrians are modelled as intelligent active Brownian particles (iABPs) in two spatial dimensions

[see Fig. 1(b), which experience a propulsion force f_p acting along their orientation vector \mathbf{e}_i , and a friction force $-\gamma\mathbf{v}_i$ with velocity \mathbf{v}_i , which implies a constant speed $v_0 = f_p/\gamma$. Each pedestrian is associated with a type t_i , which encodes their goal direction $\hat{\mathbf{d}}(t_i)$. We employ a self-steering mechanism in the form of a torque that changes the direction of motion as

$$\dot{\mathbf{e}}_i = \sqrt{2(d-1)D_r}\mathbf{\Lambda}_i + \Omega\mathbf{M}_{\text{vis}} + K\mathbf{M}_{\text{goal}}, \quad (1)$$

where D_r is the rotational diffusion coefficient, d is the dimensionality, $\mathbf{\Lambda}_i$ is a Gaussian random process, Ω and K are the strength of the vision (\mathbf{M}_{vis}) and goal-fixation (\mathbf{M}_{goal}) steering torques, respectively [see Methods for details]. The vision steering torque \mathbf{M}_{vis} aligns the orientation vector \mathbf{e} away from the center of mass of agents in the vision cone, while the goal-fixation torque \mathbf{M}_{goal} aligns \mathbf{e} with the goal vector $\hat{\mathbf{d}}(t_i)$, see Fig. 1(a). The vision-based steering torque also contains a weight factor that increases the relative importance of avoiding agents moving head-on toward each other by a factor 1/2 relative to co-moving agents [31]. The activity of the agents is described by the dimensionless Péclet number $\text{Pe} = f_p/(\gamma R_0 D_r) = v_0 \tau_r / R_0$, where $\tau_r = 1/D_r$ is the rotational diffusion time, $v_0 = f_p/\gamma$ is the agent velocity, and R_0 is the effective vision range. The system is studied for varying relative maneuverability $\Delta = \Omega/K$, vision angle ψ , and inflow rate Γ . We operate in the limit of over-damped motion, so that inertial effects are negligible and the self-steering gives a realistic description of pedestrian cognitive motion, see Fig. 1(c-f). This also avoids the conceptual problems of forced-based models which are mostly a consequence of strong inertia effects (see e.g. Ref. [32]). The agents are considered point particles, i.e. the simulations are in the limit of semi-dense crowds, where the volume-exclusion radius σ of an individual pedestrian is much smaller than the vision range R_0 , i.e. $\sigma \ll R_0$.

Dynamic State Diagram – The state diagram of the various collective pedestrian movement states as function of relative maneuverability Δ and vision angle ψ is shown in Fig. 2(a). At small $\Delta \lesssim 1$, agents essentially ignore each other and head directly toward the goal, see Fig. 2(b). This is qualitatively similar to the case of panicking pedestrian crowds, where the 'goal' becomes more important than avoidance [34]. This behaviour corresponds to the case of 'dumb' active Brownian particles, and is expected to display activity-induced jamming in the presence of excluded volume effects. Thus, efficient navigation requires pedestrians to have maneuverability Ω larger than goal fixation K , i.e. $\Delta = \Omega/K \gtrsim 1$. The required relative maneuverability Δ increases with decreasing vision angle, as agents see fewer other agents for smaller ψ . As Δ increases for larger vision angles, the pedestrian streams start to avoid each other, which results in a complex motion marked by many scattering events, see Fig. 2(d) and Movie M1. While for two intersecting streams, lane (or stripe) formation occurs [35], for three streams the scenario is much more complex and no stable global order exists [8]. The agents rapidly change their direction attempting to avoid other agents leading to noisy and convoluted trajectories. For $\psi = \pi$, agents enter a jammed-percolating state, wherein strong clustering is observed and agents cross the interaction regime in groups, see the 'clustered' trajectories in Fig. 2(c).

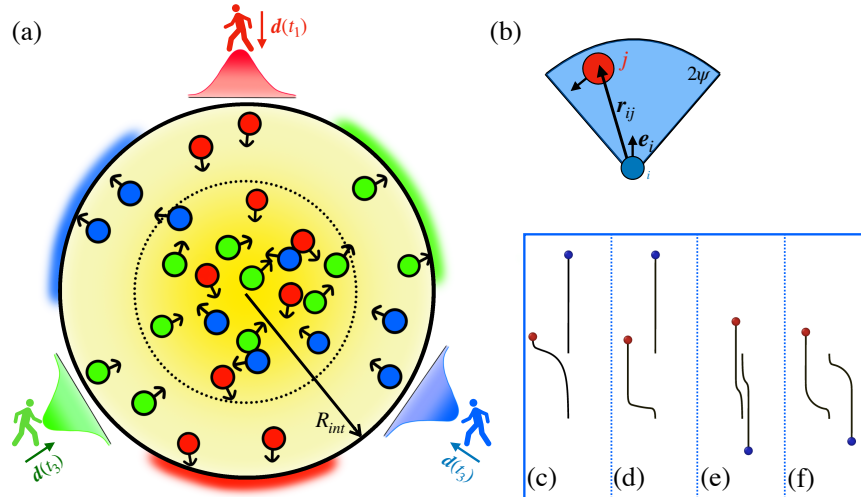


Fig. 1 (a) Simulation setup of a three-way pedestrian crossing. The colours represent different pedestrian types t_i , i.e. pedestrians with different goals [alignment along $\mathbf{d}(t_i)$]. The human markers show the position of influx, each separated by an angle of $\pi/3$ from the other and placed on an interaction circle of radius $R_{\text{int}} = 120R_0$. The shaded regions depict the regions of 'successful exits' [see Supplementary Information (SI) [33]], and the distribution at the inflow indicates the 'spread' of each stream leading to an effective interaction zone (dashed circle) $R_{\text{int}}/2$ [see Methods]. (b) Schematic diagram of the vision-based interaction of agent i with agent j . The vision angle is highlighted in blue, with a vision angle ψ and cutoff $4R_0$. Sample trajectories showing the effect of alignment and visual avoidance for a vision angle of $\psi = \pi/2$. Agents with the same goal direction for (c) $\Delta = 1$ and (d) $\Delta = 2$. The blue agent does not 'see' the red one and therefore does not react. Agents with opposite goal directions for (e) $\Delta = 1$ and (f) $\Delta = 2$. In this case, both agents see each other and move away. In all cases at $t = 0$, the distance between the agents is $r = 3R_0$.

As the vision angle is further decreased, to $\psi < \pi/2$, the particle motion drastically changes, see Fig. 2(e). In this regime, agents mainly avoid other agents directly ahead of them, implying that their direction of motion changes only for high particle densities, i.e. close to the centre of the interaction zone and near the other incoming pedestrian streams. This state is characterized by the presence of parallel trajectories in the interaction zone [see Fig. 2(e)]. Here an agent of one type initially adopts a strategy of polar alignment with the oncoming agents of the other types to avoid "collisions". The small vision angle is responsible for this flocking-based avoidance mechanism, and has been shown recently in Ref. [30]. No pronounced differences are observed for various choices of Pe across all vision angles, which is due to the large goal-fixation ($K/D_r = 8$).

Cluster-Size Distributions: Percolation and flocking – As Δ increases for vision angle $\psi = \pi$, the system undergoes a jamming transition due to increased avoidance between agents. Note that the jamming here is **not** due to volume exclusion, but due to the strong tendency to maintain a large inter-agent distance in all directions. In the jammed state, the agents crowd the interaction regime and form large clusters comprised of agents with the same goal (or type). Clustering is initiated at the inflow; the clusters then extend deep into the interaction region as agents navigate toward

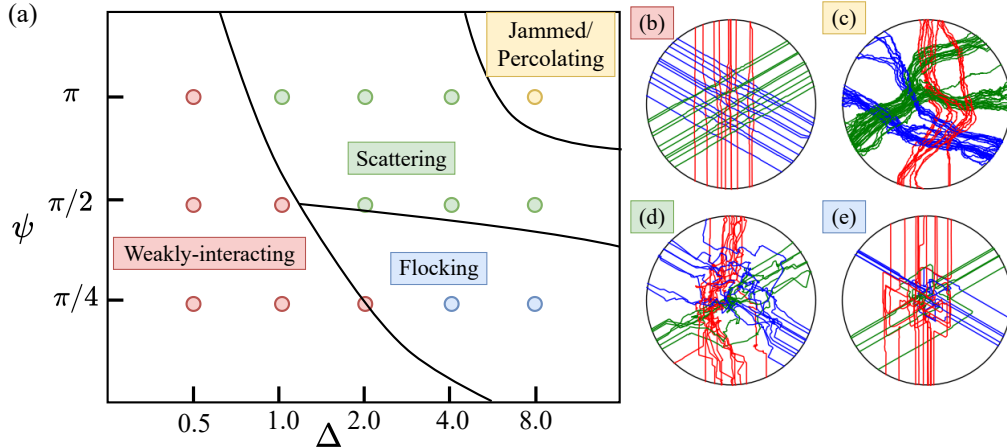


Fig. 2 (a) State diagram of pedestrian movement states as a function of the relative maneuverability $\Delta = \Omega/K$ and vision angle ψ . (b) For small Δ , the agents do not avoid each other significantly, and pass through the interaction zone nearly unhindered. (c) For higher Δ , and the largest vision angle $\psi = \pi$ and relative maneuverability $\Delta = 8$, a jammed, percolating phase develops. (d) For intermediate Δ and vision angles $\psi \geq \pi/2$, a scattering regime emerges as the agents attempt to avoid each other while crossing. (e) For intermediate Δ and smaller vision angles $\psi < \pi/2$, a 'flocking' regime is found, where agents navigate by aligning with oncoming individuals, forming a local co-moving pedestrian cluster, thus leading to clustering and flocking – as seen by the emergence of parallel trajectories (with different pedestrian types). Here we fix $\Gamma = 1$.

their respective goals. Remarkably, the jammed state also exhibits percolation, i.e. the clusters span the length of the interaction zone, see Fig. 3(a). The cluster-size distribution shows a power-law decay, with an exponent 2.2, consistent the percolation universality class [36]. Therefore, despite of the complex motion and continuously varying environment, the movement from the inflow to the exit can be understood qualitatively under the realm of percolation theory. The broad peak in the cluster-size distribution at $n_c \gtrsim 200$ represents the cluster formed initially at the inflow that then feeds smaller clusters into the system which make their way to the exit ($n_c < 100$). Note that the percolation in this case is dynamic, i.e. the system shows transient periods of percolating clusters, interrupted by times when the clusters are dispersed, see Fig. 3(b).

In the regime of small vision angles, specifically for $\psi = \pi/4$, agents exhibit avoidance-induced flocking behavior. Consider two agents moving toward each other at a small angle, so that only one of them is visible to the other. The 'aware' agent initiates a (slight) turn to avoid a collision. However, the unaffected motion of the other agent causes it to repeatedly enter the vision cone of the 'aware' agent. Consequently, the aware agent must keep turning away until the other agent is no longer visible to it. This only happens when they move essentially parallel to each other, resulting in the formation of a co-moving cluster, as illustrated in the inset of Fig. 3(c). This process repeats when this mini-cluster encounters other agents, who may also align to avoid

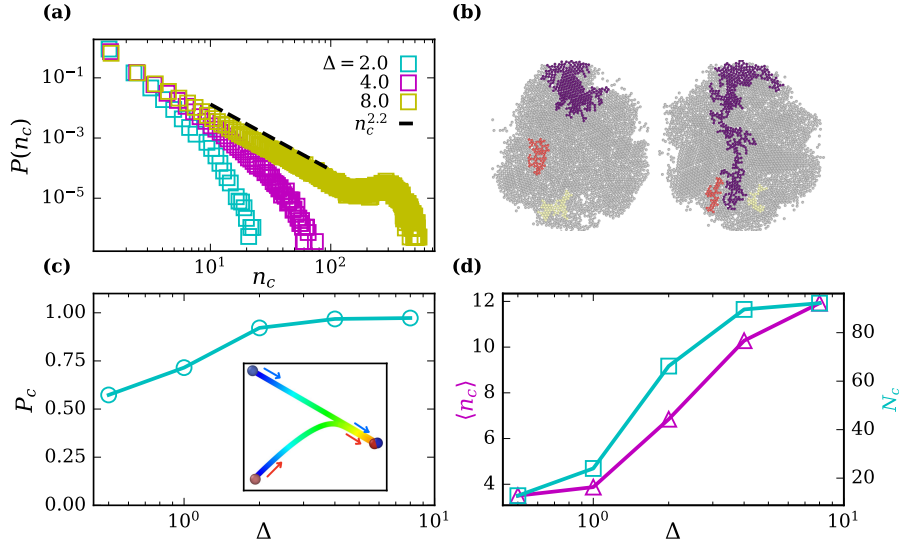


Fig. 3 (a) A phase transition into the percolation state occurs as Δ is increased for vision angle $\psi = \pi$, marked by the development of a power law decay of the cluster size distribution $p(n_c)$ and the large percolated cluster. The peak at large cluster sizes is due to finite system size. (b) The three largest clusters at $\Delta = 8.0$ and $\psi = \pi$ at two different times for pedestrians of one type. (Left) Clusters are dispersed and the largest cluster is at the inflow. (Right) The largest cluster can feed smaller clusters and reach up-to the exit, forming a transiently percolated cluster. (c) Average cluster polarization P_c [see Eq. S3 in SI] for $\psi = \pi/4$ shows an increase with Δ , indicating the development of avoidance-induced flocking. The inset shows the trajectory of two agents exhibiting avoidance-based flocking. (d) The transition into the flocking phase is characterized by a strong increase in both the mean cluster size $\langle n_c \rangle$ and the number N_c of clusters. The distance cutoff R_{cut} are chosen to be $R_{cut} \simeq R_v$ and $R_{cut} \simeq R_0$ for vision angles $\psi = \pi$ and $\psi = \pi/4$, respectively [SI].

collision, thereby also becoming part of the cluster [see Movie M2]. A particle can only leave the cluster if a strong fluctuation disrupts its aligned state. Consequently, an avoidance-induced clustering and flocking state emerges as the strength of relative maneuverability Δ increases.

This phenomenon is characterized in Fig. 3(c,d), where a significant increase in the average cluster size $\langle n_c \rangle$, number N_c of clusters, and cluster polarization P_c is observed with increasing Δ . For small $\Delta \lesssim 1$, polarization remains close to 0.5, indicating a non-flocking state. This occurs due to the random overlap of particles from neighboring streams that do not avoid each other due to the low self-steering avoidance. However, as Δ increases, the clusters achieve a polarization value near unity, signalling the emergence of a flocking/clustering state.

Path Length Distributions – With increasing relative maneuverability Δ , strong avoidance between agents leads to scattering, and implies larger exit times and broader path-length distributions, as presented in Fig. 4 for various Δ and ψ . For $\Delta \lesssim 1$, inter-agent interactions are small, and the path length distribution of nearly straight paths

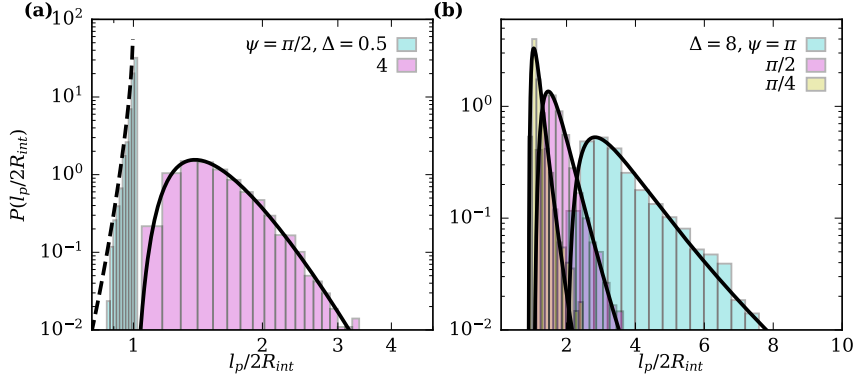


Fig. 4 Probability distribution P of the path length l_p for (a) different relative maneuverability ($\psi = \pi/2$, $Pe = 100$) and (b) different vision angles ($\Delta = 8$, $Pe = 100$). For small Δ , the paths are nearly straight and the probability distribution is well approximated by Eq. (2)[dashed line]. In scenarios characterized by high maneuverability (Δ) and large vision angles (ψ), agents traverse longer paths within the interaction sphere to navigate around others. This behavior yields a log-normal distribution for the path length, with the black solid line representing a fitted log-normal model to the data. The path lengths are only determined for trajectories that successfully reach the exit (SI) and are averaged over different agent types. The data is collected for times $4t_0 < t < 16t_0$ and averaged over all agents, where $t_0 = 2R_{int}/v_0$.

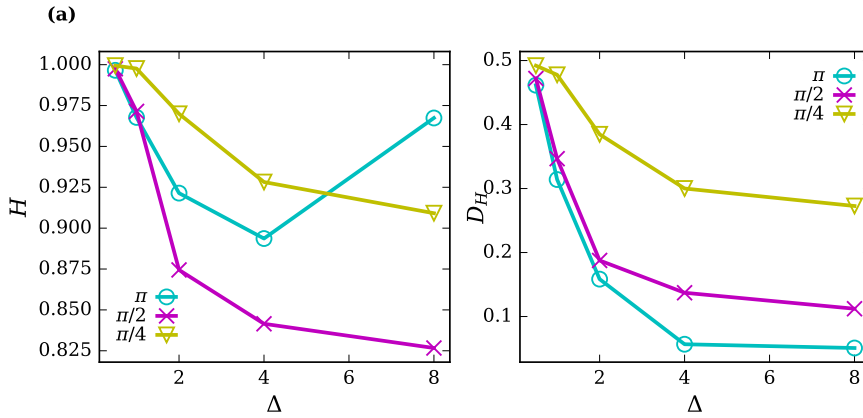


Fig. 5 The (a) Hurst exponent H and (b) diffusion coefficient D_H for increasing Δ and different vision angles ψ . The values are estimated by averaging over the two values measured by fitting Eq. (5) and Eq. (6) to $C(t)$ and MSD respectively, and averaging the values over different Pe numbers. Only trajectories that successfully reach the exit are considered and we average over all agents.

can be estimated to be [SI]

$$f_L(\tilde{l}_p) = \frac{2\tilde{l}_p \exp[-(1 - (\tilde{l}_p)^2)/2(\tilde{\sigma})^2]}{\tilde{\sigma} \sqrt{2\pi(1 - (\tilde{l}_p)^2)}}, \quad (2)$$

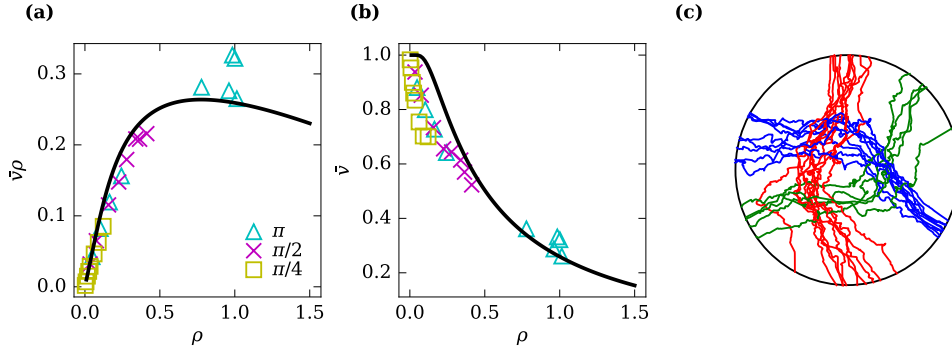


Fig. 6 Fundamental diagrams of the pedestrian flow measured by performing simulations with different pedestrian inflow Γ for a fixed $\Delta = 8$. (a) Flux $J = \bar{v}\rho$ and (b) average velocity \bar{v} as a function of the mean agent density ρ . The data collapses onto a single master curve for different vision angles and exhibits the characteristic shape of the fundamental diagram, showing the free flow ($\rho < 0.5$) and jammed regimes ($\rho > 1$). (c) Agent trajectories for $\Gamma = 4$ and $\psi = \pi/2$ showing the development of rotational flows and roundabout traffic like motion. For $\psi = \pi$, a jamming transition occurs for large inflow $\Gamma > 0.5$, marked by a sudden rise in density (see $\rho > 1.0$) and a strong reduction in velocity \bar{v} . The solid black line in (a,b) is an approximate fit based on the Kladek formula $v(\rho) = v_0[1 - \exp(-c[\rho^{-1} - \rho_{jam}^{-1}])]$, where $v_0 = 1$ and we set $\rho_{jam} = 4$ and $c = 0.4$ for a good fit.

where $\tilde{l}_p = l_p/2R_{\text{int}}$ and $\tilde{\sigma} = \sigma/R_0$ is the normalized variance at the input of the stream. For low Δ , the data matches well with the estimated distribution, see Fig. 4(a). However, as Δ increases, the distribution shifts to larger l_p and broadens. This occurs as agents scatter strongly due to high avoidance Δ , leading to longer paths. Agents with lower vision angles reach their destinations in shorter paths, due to fewer scattering events as seen in Fig. 4(b), where increasing ψ causes a shift of the distribution to larger l_p , along with the development of a longer tail. The distributions for $\Delta \gtrsim 1$ and $\psi \geq \pi/2$ follow a log-normal distribution, which is verified by performing a Kolmogorov–Smirnov test with confidence interval of 95%. Notably, log-normally distributed path lengths have been documented in antipode experiments involving pedestrians initiated on a circle [12]. The experimental arrangement closely mirrors the three-stream configuration utilized in our simulations, providing empirical support for the shape of the observed distribution.

Dynamics, Mean-Squared Displacement, and Fractional Brownian Motion – To better understand the dynamics of the agents, we compute their mean-squared displacement (MSD)

$$\langle \mathbf{r}^2(t) \rangle = \langle |\mathbf{r}(t + \tau) - \mathbf{r}(\tau)|^2 \rangle_\tau, \quad (3)$$

where $\mathbf{r}(t)$ is the position vector of the particle at time t . The MSD curves [see extended data Fig. 7] indicate that increasing Δ or ψ leads to larger scattering causing a shift of the motion from ballistic to super-diffusive. We also calculate the orientational auto-correlation function

$$C(t) = \langle \mathbf{e}_i(t + \tau) \cdot \mathbf{e}_i(\tau) \rangle_\tau \quad (4)$$

for different Δ at $\psi = \pi/2$ [see extended data Fig. 7]. For small $\Delta \lesssim 1$, the motion is strongly correlated, i.e. the particles hardly change their direction of motion as they

have a strong tendency to orient and move toward the goal and do not scatter. For $\Delta \gtrsim 1$, the auto-correlation function $C(t)$ displays a slow power-law decay, consistent with the super-diffusive behavior observed in the MSD $\langle \mathbf{r}^2(t) \rangle = K_\alpha t^\alpha$.

The observed functional forms of $C(t)$ and the MSD suggest that the motion of a single agent can be described by fractional Brownian motion [37], where the velocity auto-correlation has the form [see SI]

$$C(t) = \frac{dD_H}{\Gamma(2H-1)} t^{2H-2} \quad (5)$$

with the corresponding MSD

$$\langle \mathbf{r}^2(t) \rangle = \frac{2dD_H}{\Gamma(2H+1)} t^{2H}, \quad (6)$$

where d is the spatial dimensionality, H is the Hurst exponent and D_H measures the strength of the coloured noise. Assuming the power law decay of $C(t)$ has the form given by Eq. (5), it can be checked that the coefficient K_α and exponent α measured from the MSD match the expected values $\alpha_{th} = 2H$ and $K_{th} = 2dD_H/\Gamma(2H+1)$, with H and D_H fitted from $C(t)$ [see extended data Fig. 8]. This implies that a fractional Brownian motion of the agents well describes the scattering process. Figure 5(a) shows a marginal variation in the Hurst exponent with $0.8 < H < 1$, consistent with the super-diffusive/ballistic motion of the agents ($\alpha = 2H$). In particular, a value $H > 1/2$ indicates the long memory effect of the noise, a consequence of the goal oriented motion of the pedestrians. Notably, there is a strong decrease in D_H for increasing Δ and (or) ψ due to more scattering events, thus implying smaller diffusion coefficient $K_\alpha \propto D_H$, see Fig. 5(b). Note that in our case the 'noise' strength of the fBM is related to the average step length taken by the agent, which decreases for increased scattering. Thus an *increase* in 'scattering induced noise' causes an *decrease* in the fBM noise, an important correspondence to keep in mind. From the analysis it can be concluded that the interactions lead to an overall decrease in the effective velocity captured via D_H , while the motion is still overall 'goal-oriented' i.e super-diffusive.

Notably at $\Delta = 8$, the jammed/percolated phase for $\psi = \pi$ has a larger Hurst exponent H compared to the 'scattering' state at $\Delta = 4$ and $\psi = \pi$, despite of nearly equal diffusion coefficient D_H . Here, by moving within the percolated cluster, the agents are able to achieve directed movement with larger long-time memory effects (i.e. H) as the agents follow the cluster that has already made its way to the exit, highlighting the unique dynamics of the jammed state [see Movie M3]. Qualitatively, this phenomenon resembles the behaviour of pedestrians joining forces to penetrate through highly congested areas, reflecting a collective strategy to navigate through crowded spaces more effectively. These results are striking, as they suggest that the complex motion involving a combination of noise, goal fixation, and vision-based steering avoidance between several other agents can be described in a mean-field manner by a coloured-noise approximation.

Dependence on Inflow Rate – The (dimensionless) inflow rate Γ , i.e. the number of agents entering at the inflow region per unit time τ_r , is an important parameter that

determines the emergent behaviour in the interaction regime. Already in the much simpler scenario of single-file motion with volume exclusion, changing the inflow (and similarly the outflow) rate can lead to so-called boundary-induced phase transitions [38]. We focus on the regime of large Δ representing the case of strong avoidance, and study the effect of changing inflow rate on the agent motion for different vision angles ψ .

The fundamental diagram for the pedestrian movement relates flux $J = \rho \bar{v}$ and average velocity \bar{v} to the local density ρ , see Fig. 6(a,b). The local density $\rho = Nd_{neigh}^2/R_{int}^2$ in the interaction region (of radius $R_{int}/2$) is measured by approximating the area occupied by each agent by the average minimum separation $d_{neigh}(\Gamma, \psi)$ within the vision range R_v [see SI]. Since the motion is largely ballistic, we approximate the average velocity as $\bar{v} = \sqrt{K_\alpha}$. Notably, we observe a collapse of the data for different vision angles onto a single master curve with the characteristic form of the fundamental diagram, i.e. a free-flow regime at low ρ and the jammed state at high ρ . Even without explicit velocity adaptation in our model, we successfully replicate essential features of the fundamental diagram for pedestrian flow [39]. This implies that the model demonstrates robust properties when examined from a statistical viewpoint. Additionally, we conclude from our simulation results that the fundamental diagram holds even for different vision angles.

In the free-flow regime, we have a steady state and the inflow equals the outflow. However, at $\psi = \pi$, a jamming transition occurs around $\Gamma_{crit} \approx 0.5$, leading to a sudden rise in the local density ($\rho > 1.0$) [see extended data Fig. 9]. In this case, a large number of agents exit close to the entry due to overcrowding in the interaction regime and the outflow saturates. The jamming is triggered by the limited transport capacity in the interaction regime, and thus generally $\Gamma_{crit} = \Gamma_{crit}(R)$, where R is the system size. This is notably different from boundary-induced phase transitions in one-dimensional systems [38], which show no system-size dependence. Moreover, the monotonic decay of $\bar{v}(\rho)$ suggests that the free-flow to jamming transition may be understood as motility-induced jamming [19], where the repulsive conservative potential of standard ABPs is replaced here by a vision-assisted steering avoidance. At smaller vision angles, the system maintains the free-flow regime even at large inflow, as agents allow for closer proximity [see SI], preventing congestion. Increasing ρ (i.e. Γ) causes a decrease in the average velocity due to increased scattering in the interaction regime, as seen in Fig. 6(b). In particular for the jammed state ($\rho \gtrsim 1.0$), a sharp reduction in the velocity is seen. As before, the jammed state has a heightened value of α due to the long time persistent motion of particles within percolated clusters.

Interestingly for $\psi = \pi/2$, different movement strategies emerge as the inflow rate Γ is increased. For instance, at $\Gamma = 2.0$ and 4.0 , a rotation state develops wherein agents follow other agents with the same goal and form a vortex around the center of the interaction, see Fig. 6(c). This rotation state also allows for lower repulsion as each particle is largely aligned with the neighbors, see Eq. (11) in Methods. This motion also creates an ‘eye’ in the centre, marked by agent depletion [see extended data Fig. 9 and Movie M4], suggestive of traffic at a roundabout. This is consistent with the observation of several studies that show the stabilization of pedestrian flows at intersections in presence of an obstacle [26, 34]. Thus, the self-organized development of

the 'eye' in the centre in our simulations leads to a stabilization of flow. This emergent global state offers insights into discerning effective transport strategies contingent upon the pedestrian volume.

Summary and Conclusions – Drawing inspiration from active matter models in biophysics, we have introduced a new approach to simulating pedestrian motion, which employs a vision-based steering mechanism of agents in combination with goal fixation. Unlike the Social Force Model and its derivatives which employ conservative forces via potentials for obstacle avoidance and goal following, in this work we employ a local environment-based self-steering through torques that alter the propulsion direction of the agents. The overdamped limit of the Langevin equation mitigates artefacts arising from inertia effects and Newton's action-reaction principle, which is also inherent in force-based mechanistic pedestrian models. This allows for more realistic pedestrian motion, who 'steer' their movement direction, rather than face repulsive/attractive forces, with the former navigation strategy likely dominating in low-density scenarios. Moreover, we successfully isolate the effects of different parameters such as relative maneuverability Δ , vision angle ψ , and inflow rate Γ on the collective dynamics of the agents.

In the state diagram, four classes of motion patterns of semi-dense crowds are obtained, in which agents are weakly interacting, flocking, strongly scattering, and jamming. Notably, the jammed state for $\psi = \pi$ is characterized by percolating clusters, which qualitatively resembles the behaviour of pedestrians joining forces to penetrate through highly congested areas. Despite of large differences in the global collective behaviour, the complex interplay of inter-agent interactions and goal fixation, the observed super-diffusive motion of the agents can be explained very well using a fractional Brownian motion model, featuring highly correlated noise with long memory. For increasing inflow, agents display distinct collective behaviors based on their vision angle, such as the development of roundabout motion at $\psi = \pi/2$ and a jammed state at $\psi = \pi$. Remarkably, the fundamental flow diagram is found to be universal for different vision angles.

Our study lays the groundwork for more detailed modelling of pedestrian navigation scenarios. By introducing additional torques, e.g. related to the presence of boundaries, more complex scenarios such as navigation through channels, bottlenecks, and obstacle avoidance can be studied. An important next step will be the addition of adaptable agent velocities, particularly relevant in high-density crowd simulations. Lastly, we predict the validity of the fundamental diagram for different vision angles, which would be interesting to study experimentally.

References

- [1] Feliciani, C., Shimura, K., Nishinari, K.: Introduction to Crowd Management: Managing Crowds in the Digital Era: Theory and Practice. Springer, Cham, Switzerland (2021)
- [2] Schadschneider, A., Chraïbi, M., Seyfried, A., Tordeux, A., Zhang, J.: Pedestrian dynamics: From empirical results to modeling. *Crowd Dynamics, Volume 1: Theory, Models, and Safety Problems* **1**, 63 (2018)

- [3] Corbetta, A., Toschi, F.: Physics of human crowds. *Annu. Rev. Condens. Matter Phys.* **14**, 311–333 (2023)
- [4] Zhang, J., W.W.F.Klingsch, Schadschneider, A., Seyfried, A.: Ordering in bidirectional pedestrian flows and its influence on the fundamental diagram. *JSTAT*, 02002 (2012)
- [5] Feliciani, C., Nishinari, K.: Empirical analysis of the lane formation process in bidirectional pedestrian flow. *Phys. Rev. E* **94**, 032304 (2016)
- [6] Dong, H.-R., Meng, Q., Yao, X.-M., Yang, X.-X., Wang, Q.-L.: Analysis of dynamic features in intersecting pedestrian flow. *Chin. Phys. B* **26**(9), 098902 (2017)
- [7] Mullick, P., Fontaine, S., Appert-Rolland, C., Olivier, A.-H., Warren, W.H., Pettré, J.: Analysis of emergent patterns in crossing flows of pedestrians reveals an invariant of ‘stripe’ formation in human data. *PLoS Comput. Biol.* **18**(6), 1010210 (2022)
- [8] Bode, N.W.F., Chraïbi, M., Holl, S.: The emergence of macroscopic interactions between intersecting pedestrian streams. *Transp. Res. B Methodol.* **119**, 197 (2019)
- [9] Cao, S., Seyfried, A., Zhang, J., Holl, S., Song, W.: Fundamental diagrams for multidirectional pedestrian flows. *Journal of Statistical Mechanics: Theory and Experiment* **2017**(3), 033404 (2017)
- [10] Lian, L., Mai, X., Song, W., Richard, Y.K.K., Wei, X., Ma, J.: An experimental study on four-directional intersecting pedestrian flows. *JSTAT* **2015**(8), 08024 (2015)
- [11] Sun, L., Hao, S., Gong, Q., Qiu, S., Chen, Y.: Pedestrian roundabout improvement strategy in subway stations. *Transport* **171**, 1600073 (2018)
- [12] Xiao, Y., Gao, Z., Jiang, R., Li, X., Qu, Y., Huang, Q.: Investigation of pedestrian dynamics in circle antipode experiments: Analysis and model evaluation with macroscopic indexes. *Transp. Res. Part C Emerg.* **103**, 174–193 (2019)
- [13] Hu, Y., Zhang, J., Song, W.: Experimental study on the movement strategies of individuals in multidirectional flows. *Physica A: Statistical Mechanics and its Applications* **534**, 122046 (2019)
- [14] Martinez-Gil, F., Lozano, M., Garcia-Fernandez, I., Fernandez, F.: Modeling, evaluation, and scale on artificial pedestrians: a literature review. *ACM Computing Surveys (CSUR)* **50**, 72 (2017)
- [15] Maury, B., Faure, S.: *Crowds in Equations*. World Scientific, London, Singapore

(2019)

- [16] Boltes, M., Zhang, J., Seyfried, A.: Analysis of crowd dynamics with laboratory experiments. *The International Series in Video Computing* **11**, 67 (2013)
- [17] Gompper, G., Winkler, R.G., Speck, T., Solon, A., Nardini, C., Peruani, F., Löwen, H., Golestanian, R., Kaupp, U.B., Alvarez, L., *et al.*: The 2020 motile active matter roadmap. *J. Condens. Matter Phys.* **32**(19), 193001 (2020)
- [18] Fily, Y., Baskaran, A., Hagan, M.F.: Dynamics of self-propelled particles under strong confinement. *Soft matter* **10**(30), 5609–5617 (2014)
- [19] Cates, M.E., Tailleur, J.: Motility-induced phase separation. *Annu. Rev. Condens. Matter Phys.* **6**(1), 219–244 (2015)
- [20] Iyer, P., Winkler, R.G., Fedosov, D.A., Gompper, G.: Dynamics and phase separation of active Brownian particles on curved surfaces and in porous media. *Phys. Rev. Res.* **5**(3), 033054 (2023)
- [21] Caprini, L., Marconi, U.M.B., Wittmann, R., Löwen, H.: Dynamics of active particles with space-dependent swim velocity. *Soft Matter* **18**(7), 1412–1422 (2022)
- [22] Couzin, I.D., Krause, J., Franks, N.R., Levin, S.A.: Effective leadership and decision-making in animal groups on the move. *Nature* **433**(7025), 513–516 (2005)
- [23] Barberis, L., Peruani, F.: Large-scale patterns in a minimal cognitive flocking model: Incidental leaders, nematic patterns, and aggregates. *Phys. Rev. Lett.* **117**, 248001 (2016)
- [24] Negi, R.S., Winkler, R.G., Gompper, G.: Emergent collective behavior of active Brownian particles with visual perception. *Soft Matter* **18**(33), 6167–6178 (2022)
- [25] Negi, R.S., Winkler, R.G., Gompper, G.: Collective behavior of self-steering active particles with velocity alignment and visual perception. *Phys. Rev. Res.* **6**(1), 013118 (2024)
- [26] Ondřej, J., Pettré, J., Olivier, A.-H., Donikian, S.: A synthetic-vision based steering approach for crowd simulation. *ACM Transactions on Graphics (TOG)* **29**(4), 1–9 (2010)
- [27] Wirth, T.D., Dachner, G.C., Rio, K.W., Warren, W.H.: Is the neighborhood of interaction in human crowds metric, topological, or visual? *PNAS Nexus* **2**(5), 118 (2023)
- [28] Zhang, D., Li, W., Gong, J., Huang, L., Zhang, G., Shen, S., Liu, J., Ma, H.: HdrIm3d: A deep reinforcement learning-based model with human-like perceptron

- and policy for crowd evacuation in 3d environments. *ISPRS International Journal of Geo-Information* **11**(4), 255 (2022)
- [29] Dachner, G.C., Wirth, T.D., Richmond, E., Warren, W.H.: The visual coupling between neighbours explains local interactions underlying human ‘flocking’. *Proc. R. Soc. B* **289**(1970), 20212089 (2022)
- [30] Negi, R.S., Iyer, P., Gompper, G.: Controlling inter-particle distances in crowds of motile, cognitive, active particles. *Sci. Rep.* **14**(1), 9443 (2024)
- [31] Karamouzas, I., Skinner, B., Guy, S.J.: Universal power law governing pedestrian interactions. *Phys. Rev. Lett.* **113**(23), 238701 (2014)
- [32] Cordes, J., Chraïbi, M., Tordeux, A., Schadschneider, A.: Single-file pedestrian dynamics: a review of agent-following models. *Crowd Dynamics* **4**, 143 (2023)
- [33] Supplementary Material. [URL.will.be.inserted.by.publisher](#)
- [34] Helbing, D., Molnár, P., Farkas, I.J., Bolay, K.: Self-organizing pedestrian movement. *Environment and Planning B: Planning and Design* **28**(3), 361–383 (2001)
- [35] Helbing, D., Buzna, L., Johansson, A., Werner, T.: Self-organized pedestrian crowd dynamics: Experiments, simulations, and design solutions. *Transp. Sci.* **39**(1), 1–24 (2005)
- [36] Stauffer, D., Aharony, A.: *Introduction to Percolation Theory* (revised 2nd Edition). CRC Press, London (1994)
- [37] Mandelbrot, B.B., Van Ness, J.W.: Fractional Brownian motions, fractional noises and applications. *SIAM Review* **10**(4), 422–437 (1968)
- [38] Krug, J.: Boundary-induced phase transitions in driven diffusive systems. *Phys. Rev. Lett.* **67**, 1882 (1991)
- [39] Vanumu, L.D., Ramachandra Rao, K., Tiwari, G.: Fundamental diagrams of pedestrian flow characteristics: A review. *Eur. Transp. Res. Rev.* **9**, 1–13 (2017)

1 Methods

Model details We model pedestrians moving in a three-way crossing, as shown in Fig. 1(a), with an interaction zone of radius R_{int} . Each agent i is associated with a type t_i , which encodes their goal to reach the opposite side of the crossing. There are three pedestrian streams and correspondingly three agent types. The pedestrians are here modelled as two-dimensional intelligent active Brownian particles (iABPs) which experience a propulsion force f_p acting along their orientation vector \mathbf{e}_i . Any individual variability is incorporated as noise in the equation of motion which specifies the dynamics of the position \mathbf{r}_i of an iAPB:

$$m\ddot{\mathbf{r}}_i = f_p\mathbf{e}_i - \gamma\dot{\mathbf{r}}_i, \quad (7)$$

where m is the agent mass and γ is the friction coefficient. The dynamics of the orientation vector \mathbf{e}_i is determined by

$$\dot{\mathbf{e}}_i = \sqrt{2(d-1)D_r}\mathbf{\Lambda}_i + \Omega\mathbf{M}_{\text{vis}} + K\mathbf{M}_{\text{goal}}, \quad (8)$$

(see also Eq. (1)). The noise acts perpendicular to the direction of motion, so that

$$\mathbf{\Lambda}_i = \boldsymbol{\zeta}_i \times \mathbf{e}_i, \quad (9)$$

where $\boldsymbol{\zeta}_i$ is a Gaussian and Markovian random process with $\langle \boldsymbol{\zeta}_i(t) \rangle = 0$ and $\langle \boldsymbol{\zeta}_i(t) \cdot \boldsymbol{\zeta}_j(t') \rangle = \delta_{ij}\delta(t-t')$. The agents avoid collisions with each other via 'vision-assisted' reorientation of their propulsion direction, which is described by the torque [24]

$$\mathbf{M}_{\text{vis}} = \frac{-1}{N_i} \sum_{j \in VC} T_{ij} \left[\mathbf{e}_i \times \left(\frac{\mathbf{r}_{ij}}{|\mathbf{r}_{ij}|} \times \mathbf{e}_i \right) \right], \quad (10)$$

where $\mathbf{r}_{ij} = \mathbf{r}_j - \mathbf{r}_i$ is the displacement vector between particle i and particle j , and T_{ij} is a weight factor,

$$T_{ij} = e^{(-|\mathbf{r}_{ij}|/R_0)} [3 - \mathbf{e}_i \cdot \mathbf{e}_j] / 4, \quad (11)$$

which increases the relative importance of avoiding agents moving 'head-on' towards each other ($\mathbf{e}_i \cdot \mathbf{e}_j = -1$) as opposed to co-moving agents (i.e. $\mathbf{e}_i \cdot \mathbf{e}_j = 1$) by a factor 1/2 [31]. Lastly, $N_i = \sum_{j \in VC} T_{ij}$ is the normalization factor. The exponential distance dependence in Eq. (11) limits the range of the interaction, such that for high density of agents the effective vision range is R_0 . The sum is over all particles j that are in the vision range VC of the agent i , with

$$VC = \left\{ j \mid \frac{\mathbf{r}_{ij}}{|\mathbf{r}_{ij}|} \cdot \mathbf{e}_i \geq \cos \psi \text{ and } |\mathbf{r}_{ij}| < R_v \right\} \quad (12)$$

where ψ is the vision angle and $R_v > R_0$ the 'full' vision range. Steering toward the goal is determined by the torque

$$\mathbf{M}_{\text{goal}} = \left[\mathbf{e}_i \times \left(\hat{\mathbf{d}}(t_i) \times \mathbf{e}_i \right) \right], \quad (13)$$

where the unit vector $\hat{\mathbf{d}}(t_i)$ is direction toward the goal, with which particle i attempts to align [see Fig. 1(a)]. We define the relative maneuverability $\Delta = \Omega/K$, which measures the relative strength of visual avoidance to target alignment. The combined effect of alignment and maneuverability is shown in Fig. 1(c-f). Pedestrians navigate their movement paths based on visual cues to avoid collisions with others, by adjusting their propulsion direction. For larger relative maneuverability Δ , the agents make sharper turns, see Fig. 1(d,f). Importantly, the agents' vision-based interactions are non-reciprocal for vision angle $\psi < \pi$, see Fig. 1(c,d). Here the trailing agent notices the leading agent, but not vice versa.

All influxes are spaced at the same angular distance from each other and agents enter with frequency v_0/R_0 . At each inflow, the start position $\mathbf{r}_0 = (x_0, y_0)$ of the incoming agent on the circle is determined by first sampling a number x'_0 from a normal distribution $x'_0 \sim \mathcal{N}(0, \sigma^2)$ with zero mean and standard deviation $\sigma = \pi R_{\text{int}}/18$ to generate the intermediate point $\mathbf{r}'_0 = (x'_0, y'_0)$ using $x'^2_0 + y'^2_0 = R_{\text{int}}^2$. The desired point is then generated by a rotation, $\mathbf{r}_0 = \mathbf{R}_\theta \mathbf{r}'_0$, where $\theta = 0, 2\pi/3, -2\pi/3$ for the red, green and blue streams respectively. The value of σ determines the *approximate* interaction radius R_{eff} , via the relation $N_{\text{stream}}(6\sigma) \simeq 2\pi R_{\text{eff}}$. For our choice of $\sigma = \pi R_{\text{int}}/18$, this results in an effective minimum interaction zone of radius $R_{\text{eff}} = R_{\text{int}}/2$. An agent crossing the boundary of the interaction zone at any point is removed from the simulation (absorbing boundary). The activity of the agents is described by the dimensionless Péclet number $\text{Pe} = f_p/(\gamma R_0 D_r) = v_0 \tau_r/R_0$, where $\tau_r = 1/D_r$ is the rotational diffusion time and $v_0 = f_p/\gamma$ is the agent velocity. We operate in the overdamped limit, i.e. $m/\gamma \ll 1$ so that inertial effects are negligible and $f_p \mathbf{e}_i \approx \gamma \dot{\mathbf{r}}_i$. All lengths are measured in units of R_0 , time in units of τ_r . The goal fixation is set to $K = 8D_r$ and the vision range $R_v = 4R_0$. The parameters Δ , activity Pe , and vision angle ψ are varied. The inflow rate Γ measures the number of agents entering the interaction circle at each inflow per unit time (τ_r). Excluded volume effects are neglected, as we operate in the limit of semi-dense crowds, i.e. $\sigma \ll R_0$, where σ is the volume-exclusion radius of an individual pedestrian.

Supplementary information. Supplementary text and movie captions.

2 Extended Data

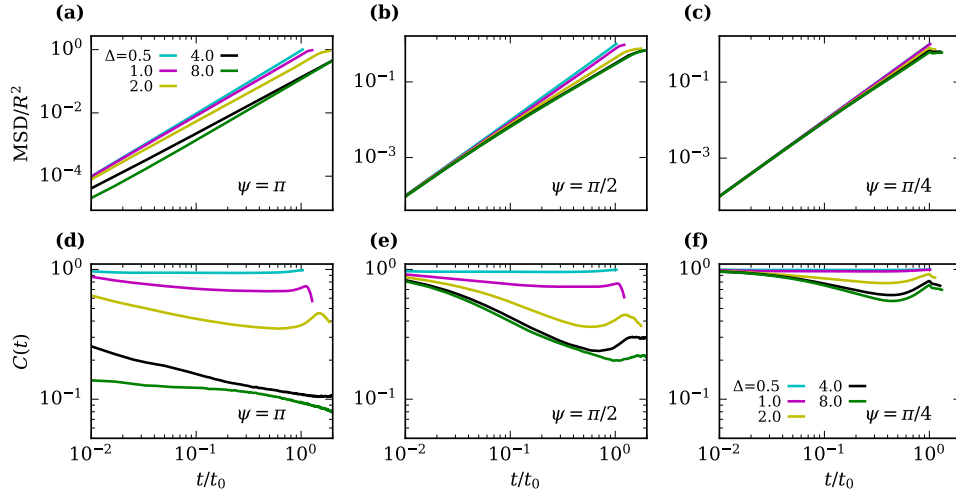


Fig. 7 Mean squared displacement (a-c) and the corresponding orientational auto-correlation function (d-f) for various Δ values at vision angles (a,d) $\psi = \pi$, (b,e) $\psi = \pi/2$, and (c,f) $\psi = \pi/4$.

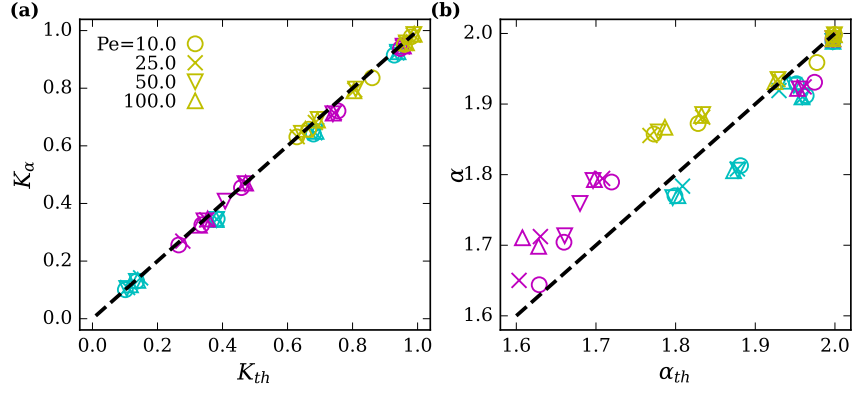


Fig. 8 (a) Measured diffusion coefficient K_α from the MSD vs. the estimated $K_{th} = 2dD_H/(\Gamma(2H+1))$ [H , D_H estimated from $C(t)$]. (b) Measured exponent α from the MSD vs the estimated $\alpha_{th} = 2H$. The different symbols correspond to different Pe number and the different colours correspond to different vision angles [π (blue), $\pi/2$ (magenta), $\pi/3$ (green)]

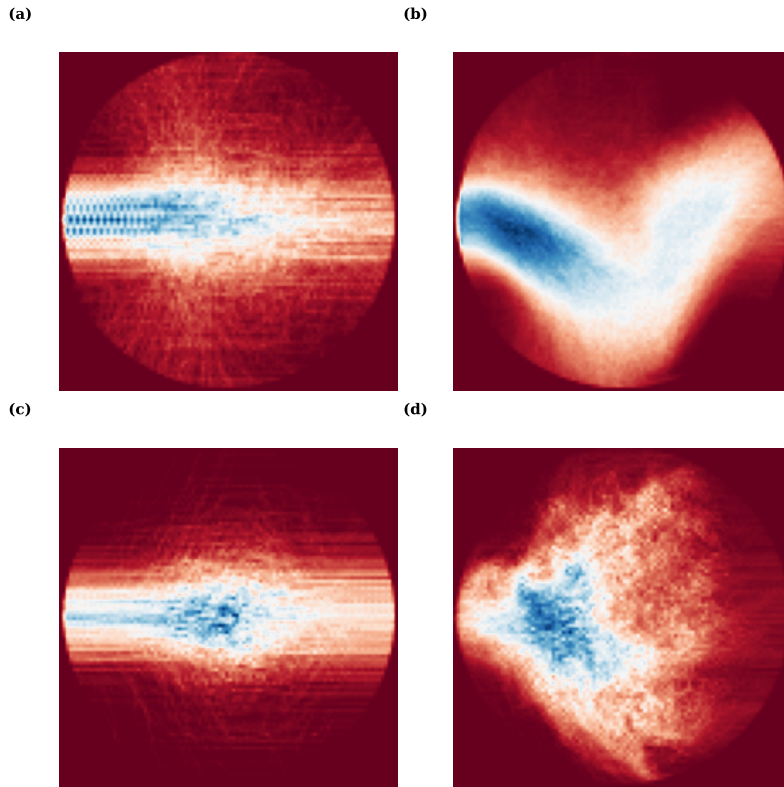


Fig. 9 Local density with varying inflow for $\psi = \pi/2$, and inflow (a) $\Gamma = 0.5$ and (b) $\Gamma = 4$. As Γ increases, a rotation phase with an asymmetric density develops, as seen in (b). Local density with varying inflow for $\psi = \pi$, and inflow (a) $\Gamma = 0.4$ and (c) $\Gamma = 0.6$. At $\Gamma = 0.4$, there is no jamming, as can be seen by the inflow and outflow density lines. However, as $\Gamma \geq 0.5$, the system enters a jammed state, characterized by the depleted outflow lines and crowding at the inflow. Here, agents enter at the left and exit at the right and the heatmap is shown for a single pedestrian stream.